CHAPTER 2

Radial Moments Based Object Recovery Under Symmetry Constraints

Mirosław Pawlak and Gurmukh Singh Panesar

In this chapter we develop a class of moment based methods for invariant image reconstruction with the selected degree of symmetry. An image function is expressed in terms of radial Zernike moments due to their invariance properties to isometry transformations and the ability to uniquely represent the salient features of the image. The regularized ridge regression estimation strategy under symmetry constraints for estimating Zernike moments is introduced. The proposed extended regularization problem allows us to enforce the bilateral symmetry in the reconstructed object. This is achieved by the proper choice of two regularization parameters controlling the level of reconstruction accuracy and the acceptable degree of symmetry. As a byproduct of our studies, we propose an algorithm for estimating an angle of the symmetry axis which in turn is used to determine the possible asymmetry present in the image. The established image recovery under the symmetry constraints model is tested in a number of experiments involving image reconstruction and symmetry estimation.

Mirosław Pawlak and Gurmukh Singh Panesar
Department of Electrical and Computer Engineering
University of Manitoba
75 Chancellor Circle
Winnipeg, Canada
e-mail: Miroslaw.Pawlak@umanitoba.ca, bm.gurmukh@gmail.com

Editor: G.A. Papakostas, *Recent Progress in Image Moments and Moment Invariants*
DOI: 10.15579/gcsr.vol7.ch2, GCSR Vol. 7, pp. 29-52, 2021

2.1 Introduction

It is commonly believed that shape defines the most important feature we perceive objects. In fact, it is the most discriminative property allowing to reconstruct, compress and classify real-world objects. In the computational shape theory one views the concept of shape as the property that can be described by measurable geometric and topological features such as area, position, orientation, distances between points, angles between lines, Euler number just to name a few [7, 11, 21]. Based on such features the fundamental problem is to define the shape equivalence involving understanding the conditions under which two distinct objects have the same shape. This question is equivalent to finding a class of transformations that when applied to an object they do not change its shape. The object transformations that preserve distance and hence shape are called isometries. In the case of 2D patterns there are four possible isometries:

1. *Translation* - the position of the object has changed.
2. *Rotation* - the orientation of the object has changed.
3. *Reflection* - the object has been folded over the line of reflection.
4. *Gliding* - the composite transformation consisting of a reflection over a line followed by translation along that line.

Formally, we say that a transformation $\mathbf{T}$ is an isometry if it preserves the distance between two points. Then, two objects f_1, f_2 are said to be congruent when there is an isometric transformation $\mathbf{T}$ such that $\mathbf{T}(f_1) = f_2$. The fundamental result of the planar geometry says that the four above listed transformations define a complete set of possible isometries for planar objects [9, 18, 16].

The concept of the isometry transformations is directly related to the property of object symmetry. In fact, symmetry is the object property that is characterized by the invariance with respect to a given isometry. Thus, we say that an object f is symmetric with respect to the isometry $\mathbf{T}$ if $\mathbf{T}(f) = f$. Hence, f is invariant with respect to $\mathbf{T}$ if applying the isometry $\mathbf{T}$ leaves the object unchanged. Specializing this definition to the reflection (bilateral) isometry with respect to a line $\mathbf{l}$ (denoted as $\mathbf{T}_{\mathbf{l}}$) we say that an object has reflection symmetry when there is a line $\mathbf{l}$ such that $\mathbf{T}_{\mathbf{l}}(f) = f$.

Furthermore, the object can be invariant (symmetric) with respect to the composition of isometries that is denoted as $\mathbf{T}_1 \circ \mathbf{T}_2$ for the isometries $\mathbf{T}_1$, $\mathbf{T}_2$. For instance, we can have that $(\mathbf{T}_{\mathbf{l_2}} \circ \mathbf{T}_{\mathbf{l_1}})f = f$, i.e., the object f is invariant with respect to the composition of two reflection transformations represented by the lines $\mathbf{l_1}$ and $\mathbf{l_2}$, respectively. It is worth noting that the transformation $\mathbf{T}_{\mathbf{l_2}} \circ \mathbf{T}_{\mathbf{l_1}}$ is equivalent to a rotation by angle 2α, where α is the angle between the lines $\mathbf{l_1}$, $\mathbf{l_2}$.

The reflection isometry and the corresponding reflection symmetry play the fundamental role in the characterization of any isometry. This is described by the following representation theorem [9, 18, 16]:

Theorem. *Any isometry can be represented as a composite of three or fewer reflections.*

The symmetry property results in the congruential class of objects that share the same set of symmetries. For instance, the letters $\{B, C, D, E\}$ share the horizontal line reflection symmetry.

In this book chapter we focus on the reflection symmetry. This is due to the aforementioned representation theorem and the fact that the reflection symmetry is the most common symmetry type in nature, human perception and various applications [17, 18, 16]. Fig.(2.1) depicts objects with the perfect reflection symmetry and the uniquely defined line of symmetry.

Figure 2.1: Objects with the perfect reflection symmetry and the unique line of symmetry.

Natural objects rarely exhibit the ideal symmetry due to various measurement errors and the inherent imperfection of the original object. Hence, symmetry should be considered as a continuous feature rather than a binary one, i.e., one should assign a degree of symmetry to a given object rather to classify it to either symmetric or non-symmetric patterns. In Fig.(2.2) we show a group of natural objects that reveal a certain degree of reflection symmetry. Within a given class of objects (like apples) the degree may vary from one object to another confirming the statistical nature of the degree of symmetry.

Quantitative analysis of the degree of asymmetry present in an object is directly related to distance between the given object and its symmetric counterpart. If the space of underlying objects has the inner product structure (Hilbert space) then the orthogonal projection of the object f onto the subspace of symmetric objects with respect to the isometry $\mathbf{T}$ is given by $\frac{f+\mathbf{T}(f)}{2}$ [20, 3]. Then, it is clear that the distance between f and its closest symmetric counterpart is

$$\left|\left|\frac{f-\mathbf{T}(f)}{2}\right|\right|, \tag{2.1}$$

where $||\cdot||$ denotes the metric in the assumed space of objects. The distance in

Eq.2.1 may serve (once it is properly normalized) as the measure of the degree of the object symmetry/asymmetry with respect to a fixed isometry $\mathbf{T}$.

Figure 2.2: Natural images revealing some degree of bilateral symmetry.

In this book chapter, we propose the radial moments based method for invariant image reconstruction with the selected degree of symmetry. This is achieved by combining the modern regression analysis with the theory of moment invariants. The proposed solution employs the ridge regression estimator augmented by the penalty function measuring the degree of object symmetry. The rest of the chapter is organized as follows. In Section 2.2 we examine the concept of reflection symmetry and the corresponding object representation in terms of invariant radial moments. In particular, the class of Zernike moments is employed. Section 2.3 defines the image observation model and examines the computing aspects of Zernike moments for digital images. Section 2.4 provides an overview of regression analysis pertinent to the theory moment invariants used in this chapter. Section 2.5 introduces our symmetry constrained reconstruction algorithm being the penalized version of the ridge regression estimate. Also an estimate of the axis of symmetry is proposed. Several experimental studies are presented to verify our methodology. In Section 2.6 we summarize our results and give further extensions.

2.2 Symmetry and Object Representation

Planar objects examined in this chapter are assumed to be identified with the bivariate function $f(x, y)$ that represents the grey-level at the location (x, y). The function is defined on a certain subset $\mathbf{D}$ of $\mathbf{R}^2$. We say that the object is mirror (reflection/bilateral) symmetric if there is an axis of symmetry that divides the image into two identical reflected images. We will identify the line of the reflection symmetry with the angle θ of the line. Formally, the image reveals the reflection symmetry if it belongs to the following class

$$\mathcal{S}(\theta) = \{f : f(x, y) = \mathbf{T}_\theta f(x, y)\}, \tag{2.2}$$

for some $\theta \in [0, \pi)$, where

$$\mathbf{T}_\theta f(x, y) = f(x\cos(2\theta) + y\sin(2\theta), x\sin(2\theta) - y\cos(2\theta))$$

is the reflection of the image $f(x, y)$ with respect to the line of symmetry defined by the angle $\theta \in [0, \pi)$. Throughout the chapter it is assumed, without loss of generality, that the coordinate system is located at the center of mass of the examined object.

It is also convenient to express the above symmetry constraint in terms of polar coordinates denoted as (ρ, φ). Hence, let $f(\rho, \varphi)$ be the version of the image function in polar coordinates. Then, the reflection symmetry transform in Eq.(2.2) reads as

$$\mathbf{T}_\theta f(\rho, \varphi) = f(\rho, 2\theta - \varphi). \tag{2.3}$$

The corresponding symmetry requirement for the image function becomes $f(\rho, \varphi) = f(\rho, 2\theta - \varphi)$ for some angle θ. Common mirror symmetry classes are: vertical symmetry ($\theta = \pi/2$), horizontal symmetry ($\theta = 0$), and diagonal symmetry ($\theta = \pi/4$). One can also consider the composition of several reflection transformations. The counterpart of Eq.(2.3) for two reflection transformations is as follows

$$(\mathbf{T}_{\theta_2} \circ \mathbf{T}_{\theta_1}) f(\rho, \varphi) = f(\rho, \varphi + 2(\theta_1 - \theta_2)), \tag{2.4}$$

where θ_1, θ_2 are the angles of symmetry lines for the first and second reflection transform, respectively. The extension of Eq.(2.4) to the three consecutive reflection transformations takes the form

$$(\mathbf{T}_{\theta_3} \circ \mathbf{T}_{\theta_2} \circ \mathbf{T}_{\theta_1}) f(\rho, \varphi) = f(\rho, 2(\theta_1 - \theta_2 + \theta_3) - \varphi). \tag{2.5}$$

As we have already mentioned the composite transformation in Eq.(2.4) defines the rotation through the angle $2(\theta_1 - \theta_2)$. Furthermore, the representation theorem characterizes any isometry of the plane in terms of a composition of at most three reflections.

In many problems related to object recognition and description it is of interest to characterize the shape of an object from indirect measurements that define the so-called shape descriptors [21]. Efficient shape descriptors should possess the following fundamental properties:

- Completeness: the descriptors should represent uniquely the object information content.
- Invariance: the descriptors should be invariant for some or all isometry transformations.
- Robustness: the descriptors should be resistant to various object degradation processes like noise, sampling and missing data.

Moments and functions of moments define shape descriptors that possess some of the aforementioned useful properties [5, 13, 21, 12]. The classical geometric moments of the so-called complex form are defined as

$$C_{pq}(f) = \iint_{\mathbf{D}} z^p z^{*q} f(x, y) dx dy,$$

where (p, q) is the moment order and $z = x + jy$, $z^* = x - jy$. Throughout the chapter it is assumed that the object domain $\mathbf{D}$ is the unit disk. Then, the polar coordinates form of $C_{pq}(f)$ is given by

$$C_{pq}(f) = \int_0^1 \int_0^{2\pi} \rho^{p+q} e^{j(p-q)\varphi} f(\rho,\varphi)\rho d\rho d\varphi. \tag{2.6}$$

This form of $C_{pq}(f)$ and Eq.(2.3) allow us to obtain the complex moment of the image reflected by the axis tilted by the angle θ. Hence, we have

$$C_{pq}(\mathbf{T}_\theta f) = e^{j(p-q)2\theta} C^*_{pq}(f). \tag{2.7}$$

Therefore, the mirror symmetry property implies that the following holds

$$e^{j(p-q)2\theta} C^*_{pq}(f) = C_{pq}(f). \tag{2.8}$$

It is also of interest to form the counterpart of Eq.(2.7) for the composition of reflection transformations. Owing to Eq.(2.4) and Eq.(2.5) we obtain

$$C_{pq}((\mathbf{T}_{\theta_2} \circ \mathbf{T}_{\theta_1})f) = e^{j(p-q)2(\theta_1-\theta_2)} C_{pq}(f) \tag{2.9}$$

and

$$C_{pq}((\mathbf{T}_{\theta_3} \circ \mathbf{T}_{\theta_1} \circ \mathbf{T}_{\theta_1})f) = e^{j(p-q)2(\theta_1-\theta_2+\theta_3)} C^*_{pq}(f), \tag{2.10}$$

correspondingly.

Since Eq.(2.9) defines the rotation by the angle $2(\theta_1-\theta_2)$ therefore one can conclude that the magnitudes $|C_{pq}(f)|$ of $C_{pq}(f)$ can be used as invariant features with respect to all rotations and reflections. This property, due to the representation theorem, also holds for all planar isometries. Nevertheless, the symmetry property in Eq.(2.8) puts some restrictions on the moment order (p,q) such that moments of certain orders are not able to discriminate between different symmetric objects [5]. Moreover, complex moments are not orthogonal and as such they do not satisfy the completeness property. Also, they lack of robustness, i.e., inability to uniquely recover the image function from noisy observations. There is also little known about the accuracy of computing $C_{pq}(f)$ from digital and noisy data.

These shortcomings of the complex moments can be overcome by the extending the definition in Eq.(2.6) to moments with respect some general class of base functions. Hence, let

$$Z_{pq}(f) = \int_0^1 \int_0^{2\pi} V^*_{pq}(\rho,\varphi) f(\rho,\varphi)\rho d\rho d\varphi, \tag{2.11}$$

be a general class of moments with respect to a class of functions $\{V_{pq}(\rho,\varphi)\}$, where $V^*_{pq}(\rho,\varphi)$ is the complex conjugate of $V_{pq}(\rho,\varphi)$ defined on the unit disk, i.e., for $0 \le \rho \le 1$, $0 \le \varphi \le 2\pi$.

Particularly attractive is the choice of $\{V_{pq}(\rho,\varphi)\}$ that forms a class of orthogonal and complete functions, i.e., when

$$\int_0^1 \int_0^{2\pi} V^*_{pq}(\rho,\varphi) V_{p'q'}(\rho,\varphi)\rho d\rho d\varphi = \lambda_{pq}\delta_{pp'}\delta_{qq'}, \tag{2.12}$$

for some constant λ_{pq} and where $\delta_{pq} = 1$ if $p = q$ and 0 otherwise.

There is a large number of orthogonal sets defined over the unit disk. One can derive a unique set by putting some symmetry conditions on $V_{pq}(\rho,\varphi)$ and additional restrictions on the indices (p,q). It was proved in [1] that a basis invariant for any rotation of axes must be of the form

$$V_{pq}(x,y) = R_p(\rho)e^{jq\varphi}, \tag{2.13}$$

where $R_p(\rho)$ is a radial orthogonal polynomial of degree p and q defines the angular order. There are various ways of selecting $R_p(\rho)$ and important examples are Fourier-Mellin, pseudo-Zernike and Zernike radial bases [5, 13]. Among the possible choices for $R_p(\rho)$ there is only one orthogonal set, the set of Zernike functions, for which $R_p(\rho) = R_{pq}(\rho)$ is the radial orthogonal polynomial of degree $p \geq |q|$ such that $p-|q|$ is even [1]. Hence, the Zernike polynomial $R_{pq}(\rho)$ has no powers of ρ lower than $|q|$. The integers p, q are the degree and the azimuth order of the polynomial $R_{pq}(\rho)$, respectively. Also note that the Zernike functions satisfy Eq.(2.12) with $\lambda_{pq} = \pi/(p+1)$. The explicit form of the Zernike radial polynomial $R_{pq}(\rho)$ can be given as it has surprising relationship to the classical Jacobi polynomials [13]. Hence, it is known that

$$R_{pq}(\rho) = \rho^{|q|}P^{(0,|q|)}_{(p-|q|)/2}(2\rho^2-1), \tag{2.14}$$

where $P^{(a,b)}_k(t)$ is the $k-$degree orthogonal Jacobi polynomial on $[-1,1]$ with the parameters $a,b > -1$. This identity leads to some useful symmetry properties of the radial Zernike polynomial $R_{pq}(\rho)$, i.e., $R_{p,-q}(\rho) = R_{pq}(\rho)$ and $R_{pq}(-\rho) = (-1)^q R_{pq}(\rho)$. Moreover, the relationship in Eq.(2.14) yields efficient algorithms for computing Zernike functions via the so-called three-term recurrent relation that is satisfied by all classical polynomial systems [6].

Figure 2.3 depicts several Zernike functions $V_{pq}(x,y)$ for various values of p,q.

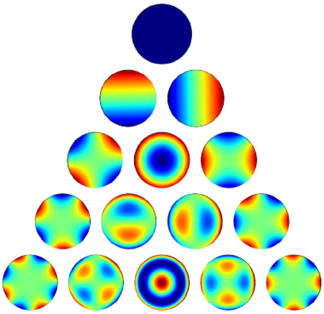

Figure 2.3: The collection of Zernike functions for various degrees p and the repetition index q.

Thus, the Zernike moment of order (p,q) is defined as

$$Z_{pq}(f) = \frac{p+1}{\pi} \int_0^{2\pi} \int_0^1 f(\rho, \varphi) e^{-jq\varphi} \, R_{pq}(\rho) \, \rho \, d\rho d\varphi, \tag{2.15}$$

where the normalization factor is included in the definition.

The fundamental property of Zernike moments is the easiness to impose the basic symmetry transformations into the radial moment formula in Eq.(2.15). In fact, applying the symmetry mappings in Eq.(2.3) to Eq.(2.15) one obtains the following relationship

$$Z_{pq}(\mathbf{T}_\theta f) = e^{-jq2\theta} Z^*_{pq}(f). \tag{2.16}$$

The counterpart of this for the composite transformations, see Eq.(2.4), Eq.(2.5), is given by

$$Z_{pq}((\mathbf{T}_{\theta_2} \circ \mathbf{T}_{\theta_1})f) = e^{jq2(\theta_1 - \theta_2)} Z_{pq}(f) \tag{2.17}$$

and

$$Z_{pq}((\mathbf{T}_{\theta_3} \circ \mathbf{T}_{\theta_2} \circ \mathbf{T}_{\theta_1})f) = e^{-jq2(\theta_1 - \theta_2 + \theta_3)} Z^*_{pq}(f). \tag{2.18}$$

By virtue of Eq.(2.16) the single reflection axis symmetry condition can be now easily expressed in terms of the Zernike moment $Z_{pq}(f)$. Hence, the image f exhibits the reflection symmetry with respect to the line of angle $\theta \in [0, \pi)$ if

$$e^{-jq2\theta} Z^*_{pq}(f) = Z_{pq}(f). \tag{2.19}$$

The analogous restriction on Zernike moments can be formulated for the composite transformations given in Eq.(2.17), Eq.(2.18).

The formula in Eq.(2.19) puts some constraints on the admissible set of Zernike moments. Hence, Eq.(2.19) holds if $Z_{pq}(f) \neq 0$ and moreover, we have

$$\arg(Z_{pq}(f)) = -q\theta. \tag{2.20}$$

In particular, this implies that if the horizontal mirror symmetry holds then $Z_{pq}(f)$ is real. The important difference between these restrictions and the ones established for complex moments is that the symmetry invariance conditions of radial moments influence only the angular order q defining the Zernike moments $\{Z_{pq}(f)\}$. Furthermore, the orthogonality property of Zernike functions allows us to group moments such that we can uniquely characterize the symmetry condition in Eq.(2.19) and in the same time to recover the image. In conclusion, the Zernike moments possess the aforementioned essential properties of completeness and invariance. This allows us to write the unique representation of the image function as the T-term expansion in terms of Zernike functions

$$f_T(x, y) = \sum_{p=0}^{T} \sum_{q=-p}^{p} Z_{pq}(f) V_{pq}(x, y), \tag{2.21}$$

where the summation is taken with respect to the admissible pairs (p, q), i.e., $p \geq |q|$ and $p - |q|$ is even. Moreover, $V_{pq}(x, y)$ can be expressed in polar coordinates as in Eq.(2.13).

It is also useful to express the representation in Eq.(2.21) in the real-valued form. To do so, one can define the real and imaginary parts of Zernike functions

$$V^r_{pq}(\rho,\varphi) = R_{pq}(\rho)\cos(q\varphi), \quad V^i_{pq}(\rho,\varphi) = R_{pq}(\rho)\sin(q\varphi) \tag{2.22}$$

for $p \geq q$, $p - q =$ even. Then, a simple algebra gives the following real-valued equivalence to Eq.(2.21)

$$f_T(\rho,\varphi) = \sum_{p=0}^{T}\sum_{q=0}^{p}\left(A_{pq}(f)\cos(q\varphi) + B_{pq}(f)\sin(q\varphi)\right)R_{pq}(\rho), \tag{2.23}$$

where $A_{pq}(f)$, $B_{pq}(f)$ are the Zernike moments corresponding to the cos and sin parts of the complex exponential, respectively. Also $p - q =$ even and $p \geq q \geq 0$. In the explicit form one obtains

$$\begin{aligned}
A_{p0}(f) &= \frac{1}{\pi}\int_0^{2\pi}\int_0^1 f(\rho,\varphi)R_{p0}(\rho)\rho d\rho d\varphi \\
A_{pq}(f) &= \frac{2(p+1)}{\pi}\int_0^{2\pi}\int_0^1 f(\rho,\varphi)\cos(q\varphi)R_{pq}(\rho)\rho d\rho d\varphi, \\
B_{p0}(f) &= 0 \\
B_{pq}(f) &= \frac{2(p+1)}{\pi}\int_0^{2\pi}\int_0^1 f(\rho,\varphi)\sin(q\varphi)R_{pq}(\rho)\rho d\rho d\varphi.
\end{aligned} \tag{2.24}$$

The formulas in Eq.(2.21), Eq.(2.23) and Eq.(2.24) can be used to obtain the equivalent $T-$term representation for the reflected image with respect to the symmetry line of the angle θ. We will denote this representation as $f^\theta_T(\rho,\varphi)$. Recalling Eq.(2.21) and the formula in Eq.(2.16) we obtain

$$f^\theta_T(\rho,\varphi) = \sum_{p=0}^{T}\sum_{q=-p}^{p} e^{-2jq\theta}Z^*_{pq}(f)V_{pq}(\rho,\varphi). \tag{2.25}$$

On the other hand the reflected counterpart of Eq.(2.23), Eq.(2.24) takes the form

$$f^\theta_T(\rho,\varphi) = \sum_{p=0}^{T}\sum_{q=0}^{p}\left(A^\theta_{pq}(f)\cos(q\varphi) + B^\theta_{pq}(f)\sin(q\varphi)\right)R_{pq}(\rho), \tag{2.26}$$

where

$$\begin{aligned}
A^\theta_{pq}(f) &= A_{pq}(f)\cos(q\pi)\cos(2q\theta) + B_{pq}(f)\cos(q\pi)\sin(2q\theta) \\
B^\theta_{pq}(f) &= A_{pq}(f)\cos(q\pi)\sin(2q\theta) - B_{pq}(f)\cos(q\pi)\cos(2q\theta).
\end{aligned} \tag{2.27}$$

are the real-valued Zernike moments of the reflected image.

It is worth noting that the L_2 distance between two images f, g can be easily expressed in term of Zernike moments. In fact, by virtue of the orthogonality and Parseval's formula one can approximate the L_2 distance $\|f-g\|^2$ as

$$\|f-g\|^2 \approx \sum_{p=0}^{T} \sum_{q=-p}^{p} |Z_{pq}(f) - Z_{pq}(g)|^2, \tag{2.28}$$

where $Z_{pq}(f)$ and $Z_{pq}(g)$ are Zernike moments of f and g, respectively.

This combined with Eq.(2.16) allows us to obtain the distance between the image function and its reflected version in terms of the Zernike moments, i.e., we have

$$\|f - \mathbf{T}_{\theta}^{\mathsf{refl}} f\|^2 \approx \sum_{p=0}^{T} \sum_{q=-p}^{p} |Z_{pq}(f) - e^{-2jq\theta} Z_{pq}^{*}(f)|^2. \tag{2.29}$$

Furthermore, applying this to Eq.(2.1) would lead to the Zernike moments based distance between the given object f and its closest symmetric counterpart (with respect to the angle θ). In fact, the distance is just $\|f - \mathbf{T}_{\theta}^{\mathsf{refl}} f\|/2$ and this due to Eq.(2.29) can be expressed in terms of the Zernike moments. Furthermore, the proper normalization of $\|f - \mathbf{T}_{\theta}^{\mathsf{refl}} f\|/2$, i.e.,

$$\mathbf{SI}(\theta) = \|f - \mathbf{T}_{\theta}^{\mathsf{refl}} f\|/2\|f\|$$

yields the symmetry index such that $\mathbf{SI}(\theta) \in [0,1]$ and $\mathbf{SI}(\theta) = 0$ if the object f is perfectly reflection symmetric with respect to the symmetry line of the angle θ.

2.3 Image Degradation and Zernike Moments Computing

In Section 2.2 we have assumed the full knowledge of the image function f defined on the unit disk. In real-world applications one does not have complete information about the image function f and must verify the question whether f reveals some type of symmetry observing only its discrete and distorted version. Hence, one observes the distorted and digital version of the image function over the pixel set $\{x_k, y_l; 1 \leq k, l \leq n\}$ according to the following model

$$Y_{kl} = \mathbb{D}f(x_k, y_l), \tag{2.30}$$

for $1 \leq k, l \leq n$, where $\mathbb{D}f(x,y)$ is a certain deformation operator. This may include noise, blurring and missing data just to name a few. For instance, the deformation consisting of linear blurring and additive noise takes the following form

$$Y_{kl} = \iint_{\mathbf{D}} \Psi(x_k - x, y_l - y) f(x,y)\,dx\,dy + \varepsilon_{kl},$$

where $\Psi(x,y)$ is the point-spread function of the given imaging system and ε_{kl} is the noise process. This image degradation model plays important role in confocal microscopy and medical imaging [5, 3, 2]. In this chapter we mostly focus on the discretization error represented by the n^2 pixels set that defines the digital image resolution. Hence, the data in Eq.(2.30) are observed on the square grid of the edge width Δ, i.e., $x_k - x_{k-1} = y_l - y_{l-1} = \Delta$ and (x_k, y_l) is the center of the pixel (k, l). Note that Δ is of order $1/n$ and the image size is $N = n^2$. In Fig.(2.4) we show the employed pixel configuration within the circular image domain. This is often referred to as the inner circle digitization [13, 19]. For the given data set in Eq.(2.30) the fundamental problem is to evaluate the Zernike moment $Z_{pq}(f)$ defined in Eq.(2.15). The numerical integration method takes the following generic form

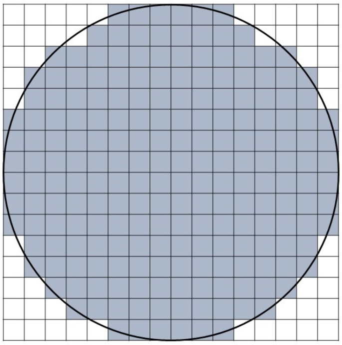

Figure 2.4: Inner circle digitization of the circular domain.

$$\widetilde{Z}_{pq} = \frac{p+1}{\pi} \sum_{k=1}^{n} \sum_{l=1}^{n} Y_{kl} \iint_{p_{kl}} V_{pq}^{*}(\rho, \varphi) \rho \, d\rho d\varphi, \tag{2.31}$$

where p_{kl} is the pixel centred at (x_k, y_l) and we used the modified notation $\widetilde{Z}_{pq}$ instead of $\widetilde{Z}_{pq}(f)$. The simplest way of evaluating the integral in Eq.(2.31) is to apply the first order integration scheme. For the higher-order integration methods we refer to [13, 15]. Thus, applying the first order numerical integration, we have the following approximation

$$\iint_{p_{kl}} V_{pq}^{*}(\rho, \varphi) \rho \, d\rho d\varphi \approx V_{pq}^{*}(\rho_k, \varphi_l) \rho_k \Delta\rho_k \Delta\varphi_l,$$

where $\Delta\rho_k = \rho_k - \rho_{k-1}$, $\Delta\varphi_l = \varphi_l - \varphi_{l-1}$. It is worth noting that the polar coordinates (ρ_k, φ_l) should be obtained from the $(x, y) \mapsto (\rho, \varphi)$ mapping that generates the polar tiling of the unit disk. The proper design of the circular domain polar tiling has an essential influence on the accuracy of Zernike moments computing. Figure 2.5 shows an example of such mapping, see [13, 19, 15] for more details.

The estimate in Eq.(2.31) has the straightforward analog for the real-valued Zernike moments defined in Eq.(2.24). The aforementioned estimates of $\{Z_{pq}(f)\}$ can be directly used to define the object reconstruction from the distorted data. Hence, the following estimate of the image function results from the combination of Eq.(2.31) and Eq.(2.21)

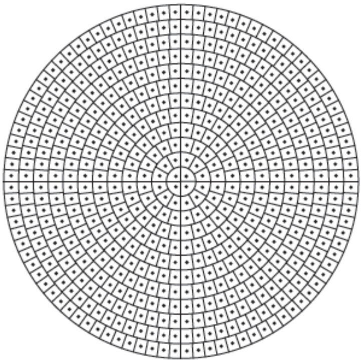

Figure 2.5: The mapping from (x, y) coordinates to polar (ρ, φ) coordinates.

$$\widetilde{f}_T(x,y) = \sum_{p=0}^{T} \sum_{q=-p}^{p} \widetilde{Z}_{pq} V_{pq}(x,y). \tag{2.32}$$

The analogous estimate can be defined for the real-valued reconstruction in Eq.(2.23).

It was shown [13, 19, 15] that under the additive white noise model the estimate $\widetilde{f}_T(x,y)$ can converge (in the mean L_2 norm sense) to the true image function with the rate $O(\Delta^{2/3})$ given that the truncation parameter T is of order $\Delta^{-2/3}$, where Δ is the pixel width. Thus, if the image resolution increases ($\Delta \to 0$) one can recover the true image with the aforementioned rate.

The method in Eq.(2.32) represents the traditional way of recovering images from the orthogonal moments as it is based on the direct estimation of the Zernike moments. This method has been extensively examined in [13, 19, 15].

In this chapter we propose the alternative approach that is utilizing modern regression algorithms like ridge regression. We will show that this leads to a more accurate reconstruction method. Moreover, the regression strategy allows us to incorporate various shape constraints such as symmetry. This is discussed in Sections 2.4 and 2.5.

2.4 Regression Analysis

Our strategy to obtain new estimates of Zernike moments is based on the extension of the standard least squares regression analysis. To do so let us re-write the reconstruction formula in Eq.(2.23) in a slightly simplified form

$$f_T(\rho,\varphi) = \sum_{p=0}^{T} \sum_{q=0}^{p} \left(A_{pq}\cos(q\varphi) + B_{pq}\sin(q\varphi)\right) R_{pq}(\rho), \tag{2.33}$$

where we used the notation A_{pq}, B_{pq} instead of $A_{pq}(f), B_{pq}(f)$. Let us assume the observation model

$$Y_{kl} = f(x_k, y_l) + \varepsilon_{kl}, \tag{2.34}$$

for $1 \leq k, l \leq n$ and $\{\varepsilon_{kl}\}$ is the zero-mean noise process. Furthermore, let us represent the pixel locations $\{(x_k, y_l)\}$ in terms of polar coordinates $\{(\rho_k, \varphi_l)\}$, see Section 2.3 for the discussion of this issue.

Then, the ordinary least squares method to estimate A_{pq}, B_{pq} is obtained by the minimization of the following criterion

$$\sum_{k,l=1}^{n} \left(Y_{kl} - \sum_{p=0}^{T} \sum_{q=0}^{p} \left(A_{pq} \cos(q\varphi_l) + B_{pq} \sin(q\varphi_l) \right) R_{pq}(\rho_k) \right)^2 \tag{2.35}$$

with respect to $\{A_{pq}, B_{pq}\}$. Here $\sum_{k,l=1}^{n}$ is the double summation with respect to all $1 \leq k, l \leq n$.

It will be useful in our future developments to rewrite the above formulas in the matrix form by introducing the vector notation. Hence, let

$$\boldsymbol{\beta} = [A_{00}, \ldots, A_{TT}, A_{20}, \ldots, A_{T0}, B_{00}, \ldots, B_{TT}, B_{20}, \ldots, B_{T0}]^t$$

where t denotes the transpose. The vector $\boldsymbol{\beta}$ consists of all the unknown coefficients $\{A_{pq}, B_{pq}; p \leq T\}$ that satisfy the restriction $p \geq q \geq 0$ and $p - q$ is even. Note that the vector $\boldsymbol{\beta}$ is $d-$dimensional with $d = (T+1)(T+2)/2$. Furthermore, let us recall the real $V_{pq}^r(\rho, \varphi)$ and imaginary $V_{pq}^i(\rho, \varphi)$ parts of the Zernike functions that are defined in Eq.(2.22). Then, one can define the following $N \times d$ matrix

$$\boldsymbol{X} = [\boldsymbol{x}_{11}, \boldsymbol{x}_{12}, \ldots, \boldsymbol{x}_{NN}]^t$$

where $N = n^2$ and

$$\begin{aligned} \boldsymbol{x}_{kl} \quad = \quad & [V_{00}^r(\rho_k, \varphi_l), V_{11}^r(\rho_k, \varphi_l), \ldots, V_{T0}^r(\rho_k, \varphi_l), \\ & V_{00}^i(\rho_k, \varphi_l), V_{11}^i(\rho_k, \varphi_l), \ldots, V_{T0}^i(\rho_k, \varphi_l)] \end{aligned}$$

is the $d-$dimensional row vector. The $N \times d$ matrix $\boldsymbol{X}$ is often referred to as the design matrix.

Finally, the observed data are summarized by the following $N-$dimensional vector

$$\boldsymbol{Y} = [Y_{11}, \ldots, Y_{1n}, Y_{21}, ..., Y_{2n}, \ldots, Y_{nn}]^t.$$

With the above notation the formula in Eq.(2.35) can be written as the classical least squares criterion

$$\boldsymbol{L}(\boldsymbol{\beta}) = ||\boldsymbol{Y} - \boldsymbol{X}\boldsymbol{\beta}||_2^2, \tag{2.36}$$

where $|| \cdot ||_2$ is the Euclidean distance. The minimum of $\boldsymbol{L}(\boldsymbol{\beta})$ is given by

$$\widehat{\boldsymbol{\beta}}_L = (\boldsymbol{X}^t \boldsymbol{X})^{-1} \boldsymbol{X}^t \boldsymbol{Y}. \tag{2.37}$$

This forms the basic estimate of the Zernike coefficients. It is known that if the noise process $\{\varepsilon_{kl}\}$ is spatially uncorrelated and equal variance σ^2 for each pixel position (k,l) then the estimate $\widehat{\boldsymbol{\beta}}_L$ is unbiased with the variance given by

$$\mathsf{Var}[\widehat{\boldsymbol{\beta}}_L] = \sigma^2(\boldsymbol{X}^t\boldsymbol{X})^{-1}. \tag{2.38}$$

The generalization of the estimate $\widehat{\boldsymbol{\beta}}_L$ to its penalized version that reveals the numerical stability and sparsity will be discussed in Section 2.5. Clearly, one could use the estimate $\widehat{\boldsymbol{\beta}}_L$ in the representation in Eq.(2.33) and to obtain the alternative reconstruction formula compared to the standard method in Eq.(2.32). The regression strategy for recovering radial moments has been rarely used in the image processing literature, see [4] for the related statistical analysis of orthogonal series estimators.

2.5 Penalized Regression Object Reconstruction and Symmetry Constraints

In this chapter we extend the classical regression analysis applied to the Zernike moments based image reconstruction to a statistical regularization method known as ridge regression. Next we examine how this modified regression strategy can incorporate symmetry constraints.

2.5.1 Ridge Regression Image Reconstruction from Zernike Moments

Thus far we have examined the case of multiple linear regression in which we assume that design matrix $\boldsymbol{X}$ is of the full rank d so that $(\boldsymbol{X}^t\boldsymbol{X})^{-1}$ exists. In our study, however, we are composing $\boldsymbol{X}$ using covariates obtained from Zernike functions up to the order T yielding the matrix of the size $N \times d$, where d is of order T^2. These covariates are collinear thus making unfeasible to use the ordinary least squares for estimating Zernike moments. The regularized version of the least squares criterion in Eq.(2.36) is a general framework to impose specific restrictions on the sought solution. Hence, in order to avoid the singularity problem of $(\boldsymbol{X}^t\boldsymbol{X})^{-1}$ one can consider the following penalized version of Eq.(2.36)

$$\boldsymbol{LR}(\boldsymbol{\beta}) = ||\boldsymbol{Y} - \boldsymbol{X}\boldsymbol{\beta}||_2^2 + \lambda||\boldsymbol{\beta}||_2^2, \tag{2.39}$$

where $\lambda \geq 0$ is a regularization parameter that controls the impact of the penalty term. The minimization of $\boldsymbol{LR}(\boldsymbol{\beta})$ yields the so-called ridge regression estimate $\widehat{\boldsymbol{\beta}}_R$ of $\boldsymbol{\beta}$ [10]. Figure (2.6) illustrates the geometry of the ridge estimate where the design matrix has substantial negative correlation. The elliptical contours correspond to the least squares term in Eq.(2.39), whereas the circular shape represents the L_2 constraint $||\boldsymbol{\beta}||_2^2 \leq \gamma$. The penalized criterion (with $\lambda \sim 1/\gamma$) is minimized at the intersection of the circle and the ellipse.

The explicit formula for the minimum of $\boldsymbol{LR}(\boldsymbol{\beta})$ in Eq.(2.39) is given by

$$\widehat{\boldsymbol{\beta}}_R = (\boldsymbol{X}^t\boldsymbol{X} + \lambda\boldsymbol{I})^{-1}\boldsymbol{X}^t\boldsymbol{Y}, \tag{2.40}$$

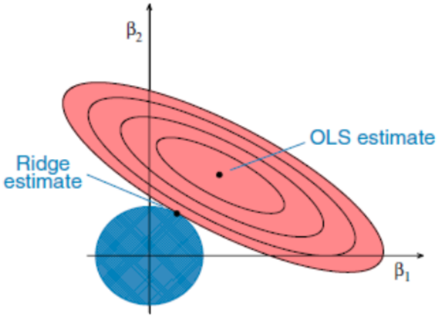

Figure 2.6: Ridge regression estimate compared with the ordinary least squares solution.

where $\boldsymbol{I}$ is the $d \times d$ identity matrix. The form of $\widehat{\boldsymbol{\beta}}_R$ explains the regularization character of the ridge regression solution. In fact, for $\lambda \to 0$, the solution is approaching the standard least squares estimate $\widehat{\boldsymbol{\beta}}_L$ in Eq.(2.37). On the other hand, for larger λ, the matrix $\boldsymbol{X}^t\boldsymbol{X} + \lambda\boldsymbol{I}$ is well defined and therefore invertible regardless whether $\boldsymbol{X}^t\boldsymbol{X}$ has rank smaller than d. This provides some degree of robustness to the ordinary least squares solution as small changes in the design matrix $\boldsymbol{X}$ may lead to large changes in $(\boldsymbol{X}^t\boldsymbol{X})^{-1}$. To get further insight into the ridge regression solution let us determine formulas for the bias and variance of $\widehat{\boldsymbol{\beta}}_R$. First, let us observe that

$$\widehat{\boldsymbol{\beta}}_R = (\boldsymbol{X}^t\boldsymbol{X} + \lambda\boldsymbol{I})^{-1}\boldsymbol{X}^t\boldsymbol{X}\widehat{\boldsymbol{\beta}}_L. \tag{2.41}$$

Then, by virtue of the aforementioned properties of $\widehat{\boldsymbol{\beta}}_L$ one can obtain

$$\mathbb{E}[\widehat{\boldsymbol{\beta}}_R] = (\boldsymbol{X}^t\boldsymbol{X} + \lambda\boldsymbol{I})^{-1}\boldsymbol{X}^t\boldsymbol{X}\boldsymbol{\beta} \tag{2.42}$$

and

$$\mathrm{Var}[\widehat{\boldsymbol{\beta}}_R] = \sigma^2\boldsymbol{A}\boldsymbol{X}^t\boldsymbol{X}\boldsymbol{A}^{-1}, \tag{2.43}$$

where $\boldsymbol{A} = (\boldsymbol{X}^t\boldsymbol{X} + \lambda\boldsymbol{I})^{-1}$. The formula in Eq.(2.42) explains the shrinkage property of the ridge regression estimate. In fact, due to the orthogonality property in Eq.(2.12) the matrix $\boldsymbol{X}^t\boldsymbol{X}$ is approximately diagonal. In fact, it can be proved [2] that

$$\sum_{(x_k,y_l)\in\boldsymbol{D}} V^*_{pq}(x_k,y_l)V^*_{p'q'}(x_k,y_l)\Delta^2$$

is equal to

$$\frac{\pi}{p+1}\lambda_{pq}\delta_{pp'}\delta_{qq'} + O(\Delta^{1+\delta})$$

for some $0 < \delta < 1$. This represents the discrete orthogonality property being the counterpart of Eq.(2.12). By this and by the comparison of Eq.(2.37) with Eq.(2.40) we approximately have

$$\widehat{\boldsymbol{\beta}}_R = \frac{1}{1+\lambda}\widehat{\boldsymbol{\beta}}_L. \tag{2.44}$$

Since $\lambda > 0$, therefore the ridge regression estimate of the Zernike moments would shrink towards zero all small moment values as compared to the standard least squares solution. Furthermore, by the same reasoning as in Eq.(2.44) and the identity in Eq.(2.43) we can conclude that the estimate $\widehat{\boldsymbol{\beta}}_R$ has smaller variability than the estimate $\widehat{\boldsymbol{\beta}}_L$. In the case of natural images one is dealing with high-dimensional data and also the collinearity of the design matrix $\boldsymbol{X}$ is common. As a result, the variance is a dominating term of the mean square error of the estimate $\widehat{\boldsymbol{\beta}}_R$ and this indicates that the regularization is necessary.

The ridge parameter λ can be selected by the $V-$fold cross validation and this provides the proper variance/bias tradeoff.

If $\boldsymbol{X}^t\boldsymbol{X}$ is approximately diagonal, then by using Eq.(2.42) and Eq.(2.43) it is straightforward to write the formula for the mean square error of the estimate $\widehat{\boldsymbol{\beta}}_R$. In fact, we have the following bias/variance decomposition

$$\mathbb{E}\left[||\widehat{\boldsymbol{\beta}}_R - \boldsymbol{\beta}||_2^2\right] = \frac{\lambda^2}{(1+\lambda)^2}||\boldsymbol{\beta}||_2^2 + \frac{d}{(1+\lambda)^2}\sigma^2. \tag{2.45}$$

We note that the first term (representing the estimate bias) is increasing with λ, whereas the second term (representing the estimate variance) is decreasing with λ. Minimization of Eq.(2.45) leads to the explicit form for the optimal λ, i.e., we have

$$\lambda^* = \frac{d}{||\boldsymbol{\beta}||_2^2}\sigma^2. \tag{2.46}$$

The true value of $\boldsymbol{\beta}$ in the above expression can be replaced by some pilot estimate, e.g., the ridge regression estimate with $\lambda = 1$. On the other hand the noise variance σ^2 can be evaluated by a class of universal techniques utilizing the difference of observations [2, 3]. This would lead to the explicit and practical estimate of λ.

The aforementioned examination produces the efficient ridge regression estimate $\widehat{\boldsymbol{\beta}}_R$ of the Zernike moments. This plugged into the reconstruction formula in Eq.(2.33) defines the ridge regression based estimate $\widehat{f}_T(x,y)$ of $f(x,y)$.

It is informative to compare this reconstruction algorithm with the standard numerical integration based method $\widetilde{f}_T(x,y)$ introduced in Eq.(2.32). Figures (2.7), (2.8) show the reconstruction of the Lena and Mandril images for increasing values of the truncation parameter T, where the image resolution is 100×100. Similar experiments were conducted for a larger class of natural images revealing the great advantage of the ridge regression reconstruction method over the traditional one. This is summarized in Fig.(2.9) where the reconstruction error versus the maximal moment order T is plotted for the assumed class of images.

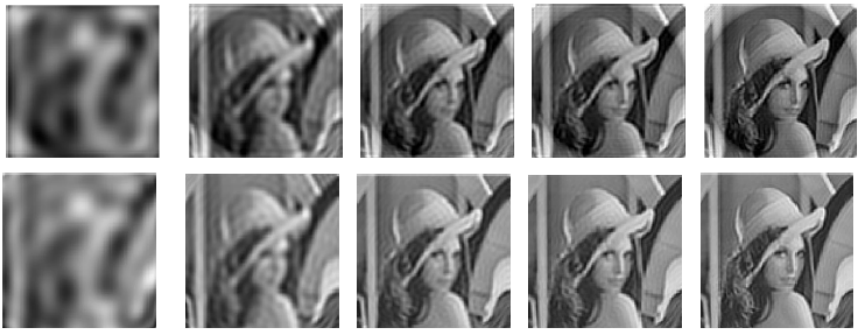

Figure 2.7: Image reconstruction based on the standard method $\widetilde{f}_T(x,y)$ (top panel) in Eq.(2.32) and the ridge regression method $\widehat{f}_T(x,y)$ (lower panel).

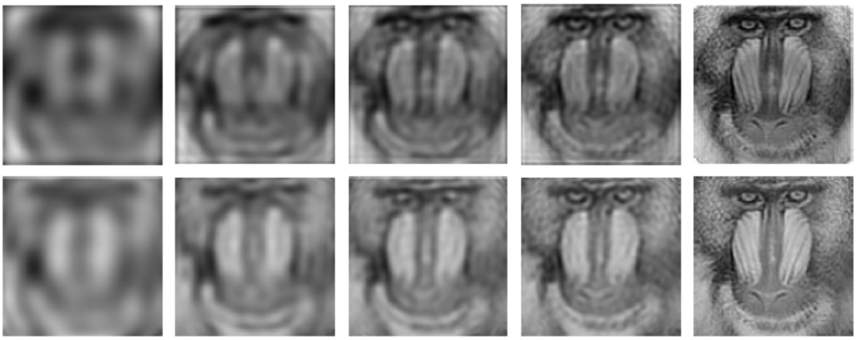

Figure 2.8: Image reconstruction based on the standard method $\widetilde{f}_T(x,y)$ (top panel) in Eq.(2.32) and the ridge regression method $\widehat{f}_T(x,y)$ (lower panel).

2.5.2 Image Reconstruction with Enforced Symmetry

In this section we wish to further extend the penalized regression analysis to the form that allows to incorporate the symmetry constraints. Hence, for the fixed axis of reflection symmetry parametrized by the angle θ let us define the following risk function

$$\boldsymbol{LRS}(\boldsymbol{\beta}) = ||\boldsymbol{Y} - \boldsymbol{X}\boldsymbol{\beta}||_2^2 + \lambda||\boldsymbol{\beta}||_2^2 + \lambda_s||\boldsymbol{\beta} - \boldsymbol{\beta}(\theta)||_2^2, \tag{2.47}$$

where $\boldsymbol{\beta}(\theta)$ is the version of $\boldsymbol{\beta}$ corresponding to the reflected image with respect to the single symmetry line of angle θ. Furthermore, $\lambda_s \geq 0$ is the regularization parameter that is controlling the degree of symmetry we wish to accept in the reconstructed image. Clearly, if $\lambda_s = 0$ then we recover the ridge regression risk function

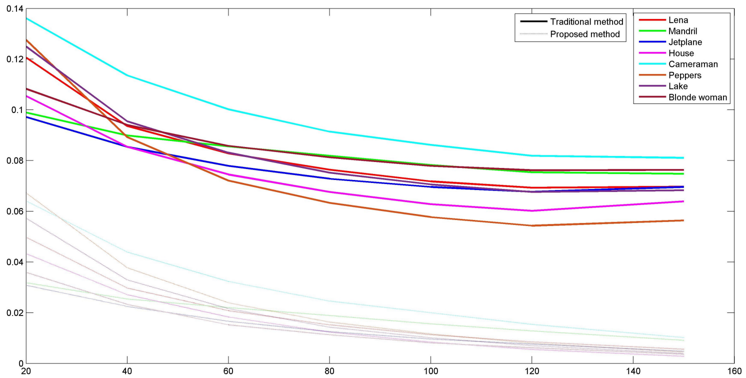

Figure 2.9: Reconstruction error for the standard reconstruction method $\widetilde{f}_T(x,y)$ and the ridge regression estimate $\widehat{f}_T(x,y)$ versus T for a large class of natural images.

in Eq.(2.39).

The formula for the transformed $\boldsymbol{\beta}(\theta)$ results from equations given in Eq.(2.27). This can be written in the matrix form as

$$\boldsymbol{\beta}(\theta) = \boldsymbol{T}(\theta)\boldsymbol{\beta}, \tag{2.48}$$

where $\boldsymbol{T}(\theta)$ is the $d \times d$ matrix having the block-wise structure. Owing to Eq.(2.27) the (p,q) block is of the form

$$\begin{bmatrix} \cos(q\pi)\cos(2q\theta) & \cos(q\pi)\sin(2q\theta) \\ \cos(q\pi)\sin(2q\theta) & -\cos(q\pi)\cos(2q\theta) \end{bmatrix}.$$

The direct minimization of $\boldsymbol{LRS}(\boldsymbol{\beta})$ yields the following double regularized estimate of the Zernike moments

$$\widehat{\boldsymbol{\beta}}_{RS} = \left(\boldsymbol{X}^t\boldsymbol{X} + \lambda\boldsymbol{I} + \lambda_s(\boldsymbol{I} - \boldsymbol{T}(\theta))^t(\boldsymbol{I} - \boldsymbol{T}(\theta))\right)^{-1}\boldsymbol{X}^t\boldsymbol{Y}. \tag{2.49}$$

Clearly, for $\lambda_s = 0$ we obtain the ridge regression estimate $\widehat{\boldsymbol{\beta}}_R$. As we have already observed the ridge regression tuning parameter λ plays the important role in reducing the variance of the ridge regression estimate. On the other hand, the symmetry regularization parameter λ_s controls the shape property of the reconstructed image in terms of its degree of bilateral symmetry, i.e., we impose the constraint $||\boldsymbol{\beta} - \boldsymbol{\beta}(\theta)||_2^2 \leq \gamma_s$, where $\lambda_s \sim 1/\gamma_s$. Hence, larger λ_s yields the solution with a larger degree of symmetry. The symmetry tuning parameter λ_s can be set by the user or selected based on a preliminary symmetry testing procedure. In the latter case one should perform a formal testing and use the result of the test to choose the proper value of λ_s. Hence, if the symmetry hypothesis is rejected then λ_s should be small, otherwise the larger value of λ_s is recommended. Hence, the power of the symmetry test should indicate the value of λ_s. Further details of the hypothesis testing driven approach for selecting λ_s will be studied elsewhere. We refer to [2, 14] for the theory of testing for image symmetries.

The estimate $\widehat{\boldsymbol{\beta}}_{RS}$ in Eq.(2.49) used in Eq.(2.23) yields to the image reconstruction formula $\widehat{f}_T(x, y; \lambda_s)$ parametrized by λ_s, where we assume that the ridge parameter λ was already specified. As we have already discussed $\widehat{f}_T(x, y; 0)$ gives the ridge regression estimate $\widehat{f}_T(x, y)$ that is not symmetry regularized. The estimate $\widehat{f}_T(x, y; \lambda_s)$ with increasing λ_s leads to a nested sequence of image estimates with the larger degree of symmetry.

To verify the usefulness of the reconstruction method $\widehat{f}_T(x, y; \lambda_s)$ we choose a class of images with varying levels of visual asymmetry as it is shown in Fig.(2.10). For instance, the butterfly image is almost perfectly symmetric while the other images reveal only the partial symmetry. The ellipse shape with the symmetry line lying outside the image is entirely non-symmetric.

Figure 2.10: Testing images with various degrees of bilateral symmetry.

The simulation results are obtained for the following range of $\lambda_s \in \{100, 200, 300, 400, 500\}$. The Zernike moments of the maximum order $T = 100$ were employed. Figure (2.11) shows reconstructed images as a result of enforcing bilateral symmetry as well as the effect of the increasing values of λ_s. The line of symmetry, i.e., the parameter θ was selected based on the method examined in the next section.

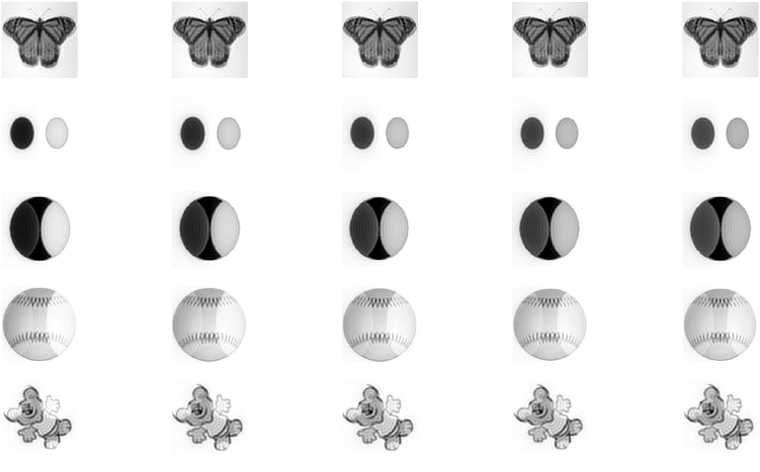

Figure 2.11: The symmetry regularized Zernike moments reconstruction method $\widehat{f}_T(x, y; \lambda_s)$ with the increasing values of λ_s.

Figure (2.12) depicts the square error (versus λ_s) between reconstructed image using $\widehat{f}_T(x, y; \lambda_s)$ and its reflected version obtained with respect to the selected symmetry axis. This represents the amount of asymmetry present in the given image. The plotted curves tend to flatten as λ_s increases beyond a certain value. Clearly, the fastest decrease of the asymmetry curves is observed for the butterfly image as being the most symmetric. The bear image in Fig.(2.10) is an example of the pattern with missing data. It is interesting to note that the symmetry driven regularization is able to recover the missing information.

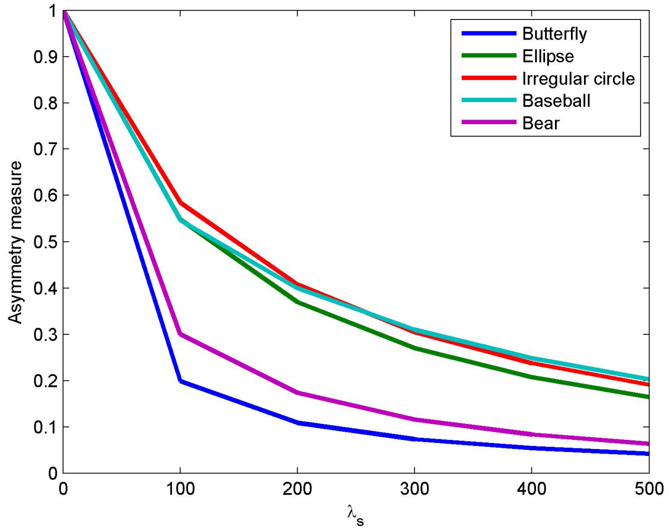

Figure 2.12: Symmetrization index versus λ_s.

Owing to the formulas in Eq.(2.4) and Eq.(2.5) one could extend our symmetry regularization theory to multiple reflection lines. The case of two reflection symmetry lines with angles θ_1, θ_2, see Eq.(2.4) and Eq.(2.17), would allow to tackle the rotation symmetry through the angle $2(\theta_1 - \theta_2)$. In this situation the regularization parameter λ_s should only depend on the difference $|\theta_1 - \theta_2|$ as the composition of the two reflections $\mathbf{T}_{\theta_2} \circ \mathbf{T}_{\theta_1}$ remains unchanged with respect to any fixed rotation.

2.5.3 Symmetry Axis Estimation

Thus far, the choice of the angle θ of reflection symmetry was set arbitrary or left to the user that can specify θ based on some a priori information about the examined class of objects. In this section we wish to give the automatic, data-driven choice of θ. In order to find the proper θ we can use some measure of the disagreement between moments of the given image and its reflected version with respect to a given value of θ. A natural such measure is defined in Eq.(2.29) which due to Parseval's formula can be expressed in terms of Zernike moments. This leads to the following symmetry distance

$$\boldsymbol{C}(\theta) = ||\boldsymbol{\beta} - \boldsymbol{\beta}(\theta)||_2^2. \tag{2.50}$$

This is clearly equal to the symmetry penalty term in Eq.(2.47), where $\boldsymbol{\beta}(\theta)$ is the version of $\boldsymbol{\beta}$ corresponding to the reflected image with respect to the line parametrized by the angle θ.

Since we have estimated the Zernike moments $\boldsymbol{\beta}$ by the ridge regression method therefore we can replace $\boldsymbol{\beta}$ in Eq.(2.50) by the ridge regression estimate $\widehat{\boldsymbol{\beta}}_R$. The ridge regression tuning parameter λ can be specified in the way as it was discussed in the previous subsection, see Eq.(2.46).

Since by virtue of Eq.(2.48) we have $\boldsymbol{\beta}(\theta) = \boldsymbol{T}(\theta)\boldsymbol{\beta}$ therefore an estimate $\widehat{\theta}$ of the angle of the symmetry axis is the value of θ minimizing the following empirical counterpart of $\boldsymbol{C}(\theta)$

$$\widehat{\boldsymbol{C}}(\theta) = ||\widehat{\boldsymbol{\beta}}_R - \boldsymbol{T}(\theta)\widehat{\boldsymbol{\beta}}_R||_2^2. \tag{2.51}$$

The above minimization problem is one dimensional and can be easily solved by either plotting $\widehat{\boldsymbol{C}}(\theta)$ or by applying some efficient minimization algorithm for single variable functions such as the golden section search method.

Figures (2.13), (2.14) depict the results of using the above approach for the symmetry angle estimation. Images with different values of the angle of symmetry have been applied. The lower panel in the both figures plots $\widehat{\boldsymbol{C}}(\theta)$ versus θ revealing local and global minima of the symmetry distance function. The point of the global minima yields our estimate $\widehat{\theta}$.

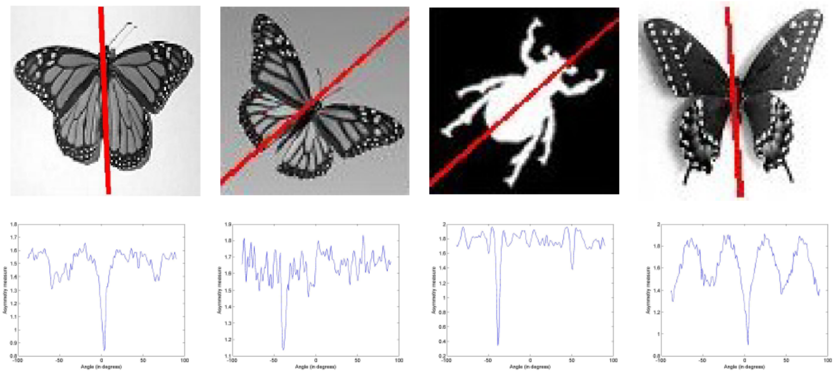

Figure 2.13: Symmetry line estimation.

The statistical precision of the estimate $\widehat{\theta}$ minimizing Eq.(2.51) would be an important problem for future research. In [3, 14] the theory of estimating θ was established, where the standard method of estimating Zernike moments, see Eq.(2.31), was employed. Based on these results one can conjecture that the estimate $\widehat{\theta}$ has some favourable statistical properties. Hence, we can expect that it reveals the optimal parametric rate, i.e.,

$$\widehat{\theta} = \theta^* + O_P(\Delta),$$

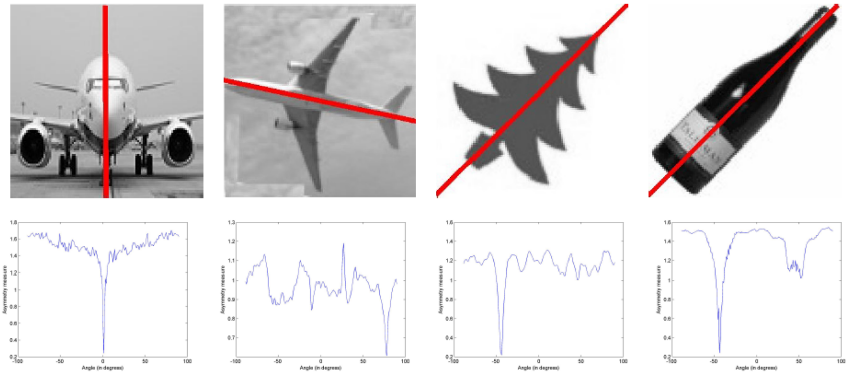

Figure 2.14: Symmetry line estimation.

where Δ is the edge width of the digital image with the resolution $n \times n$, i.e., Δ is of order $1/n$. Here θ^* denotes the true unique angle of reflection symmetry. Also, the symbol $O_P(\cdot)$ denotes the convergence in probability. This is the challenging semi-parametric estimation problem as the image function $f(x, y)$ is unknown and has the nonparametric nature.

2.6 Concluding Remarks and Extensions

In this chapter we developed the unified Zernike moments based penalized regression framework for object reconstruction with the imposed degree of symmetry. This strategy has many potential applications in object recognition, compression and understanding. It is plain that many questions, both theoretical and implementation type, remain to be addressed. First, we have examined the single reflection axis symmetry regularization. Since, as it was stated in Section 2.1 (the representation theorem) any isometry is represented by no more than three reflections, therefore it is logical to extend our theory to isometries that are composition of two or three reflections. This would cover three other isometries, i.e., translation, rotation and gliding provided that one would allow a more flexible configuration of reflection mapping lines [9]. Thus, the lines that not only intersect at a common point but the lines that are parallel and the case with two parallel lines and the line that is perpendicular to them.

Our regression strategy for estimating Zernike moments has relied on the L_2 penalized ridge regression method. The natural modification would apply the L_1 penalty. This leads to the Lasso [8] type symmetry enforced risk function

$$\boldsymbol{LLS}(\boldsymbol{\beta}) = ||\boldsymbol{Y} - \boldsymbol{X}\boldsymbol{\beta}||_2^2 + \lambda||\boldsymbol{\beta}||_1 + \lambda_s||\boldsymbol{\beta} - \boldsymbol{\beta}(\theta)||_2^2, \tag{2.52}$$

where $||\boldsymbol{\beta}||_1$ is the L_1 norm of $\boldsymbol{\beta}$. The Lasso type estimate that minimizes $\boldsymbol{LLS}(\boldsymbol{\beta})$ would allow for some degree of sparsity controlled by the parameter λ. The sparse solution would set to zero some insignificant Zernike moments and in the same time would allow for a certain degree of symmetry. The issue of controlling the proper balance between the sparsity and symmetry is left for future research.

Acknowledgment

The work of Mirosław Pawlak was supported in part by the Polish National Science Centre under Grant DEC- 2017/27/B/ST7/03082 and in part by the NSERC under Grant 319732.

References

[1] A. B. Bhatia and E. Wolf. On the circle polynomials of Zernike and related orthogonal sets. *Proceedings of Cambridge Philosophical Society*, 50:40–48, 1954.

[2] N. Bissantz, H. Holzmann, and M. Pawlak. Testing for image symmetries-with application to confocal microscopy. *IEEE Transactions on Information Theory*, 55:1841–1855, 2009.

[3] N. Bissantz, H. Holzmann, and M. Pawlak. Improving PSF calibration in confocal microscopic imaging - estimating and exploiting bilateral symmetry. *The Annals of Applied Statistics*, 4:1871–1891, 2010.

[4] H. Dette and D. P. Wiens. Robust design for series estimation. *Computational Statistics and Data Analysis*, 52:4305–4324, 2008.

[5] J. Flusser, T. Suk, and B. Zitova. *2D and 3D Image Analysis by Moments*. John Wiley and Sons, 2017.

[6] W. Gautschi. *Orthogonal Polynomials: Computation and Approximation*. Oxford University Press, 2004.

[7] U. Grenander and M. Miller. *Pattern Theory: From Representation to Inference*. Oxford University Press, 2007.

[8] T. Hastie, R. Tibshirani, and M. Wainwright. *Statistical Learning with Sparsity: The Lasso and Generalizations*. CRC Press, 2015.

[9] S.G. Hoggar. *Mathematics of Digital Images*. Cambridge University Press, 2006.

[10] G. James, D. Witten, T. Hastie, and R. Tibshirani. *An Introduction to Statistical Learning*. Springer, 2013.

[11] D. Mumford and A. Desolneux. *Pattern Theory: The Stochastic Analysis of Real World Signals*. A.K. Peters, 2010.

[12] G.A. Papakostas. *Moments and Moment Invariants: Theory and Applications*. Science Gate Publishing, 2014.

[13] M. Pawlak. *Image Analysis by Moments*. Publishing House of Technical University of Wroclaw, 2006.

[14] M. Pawlak. Moment invariants for image symmetry estimation and detection. *Moments and Moment Invariants: Theory and Applications, Ed. G.A. Papakostas*, 4:91–110, 2014.

[15] M. Pawlak and S. Liao. On the recovery of a function on a circular domain. *IEEE Transactions on Information Theory*, 48:2736–2753, 2002.

[16] J. Rosen. *Symmetry in Science: An Introduction to the General Theory*. Springer-Verlag, 1995.

[17] M.S. Treder. Behind the looking-glass: A review on human symmetry perception. *Symmetry*, 2:1510–1543, 2010.
[18] H. Weyl. *Symmetry*. Princeton University Press, 1952.
[19] Y. Xin, M. Pawlak, and S. Liao. Accurate computation of Zernike moments in polar coordinates. *IEEE Transactions on Image Processing*, 16:581–587, 2007.
[20] H. Zabrodsky, S. Peleg, and D. Avnir. Symmetry as a continuous feature. *IEEE Transactions on Pattern Analysis and Machine Intelligence*, 17:1154–1166, 1995.
[21] D. Zhang and G. Lu. Review of shape representation and description techniques. *Pattern Recognition*, 37:1–19, 2004.